

AugMapNet: Improving Spatial Latent Structure via BEV Grid Augmentation for Enhanced Vectorized Online HD Map Construction

Thomas Monninger^{1,2} Md Zafar Anwar¹ Stanislaw Antol¹ Steffen Staab^{2,3} Sihao Ding¹

¹Mercedes-Benz Research & Development North America, USA

²University of Stuttgart, Germany

³University of Southampton, United Kingdom

Abstract

Autonomous driving requires understanding infrastructure elements, such as lanes and crosswalks. To navigate safely, this understanding must be derived from sensor data in real-time and needs to be represented in vectorized form. Learned Bird’s-Eye View (BEV) encoders are commonly used to combine a set of camera images from multiple views into one joint latent BEV grid. Traditionally, from this latent space, an intermediate raster map is predicted, providing dense spatial supervision but requiring post-processing into the desired vectorized form. More recent models directly derive infrastructure elements as polylines using vectorized map decoders, providing instance-level information. Our approach, **Augmentation Map Network** (AugMapNet), proposes latent BEV feature grid augmentation, a novel technique that significantly enhances the latent BEV representation. AugMapNet combines vector decoding and dense spatial supervision more effectively than existing architectures while remaining easy to integrate compared to other hybrid approaches. It additionally benefits from extra processing on its latent BEV features. Experiments on nuScenes and Argoverse2 datasets demonstrate significant improvements on vectorized map prediction of up to 13.3% over the StreamMapNet baseline on 60 m range and greater improvements on larger ranges. We confirm transferability by applying our method to another baseline, SQD-MapNet, and find similar improvements. A detailed analysis of the latent BEV grid confirms a more structured latent space of AugMapNet and shows the value of our novel concept beyond pure performance improvement. The code can be found at <https://github.com/tmonnin/augmapnet>.

1. Introduction

Autonomous driving relies on an accurate representation of the static infrastructure surrounding the autonomous vehicle to understand the environment and make informed de-

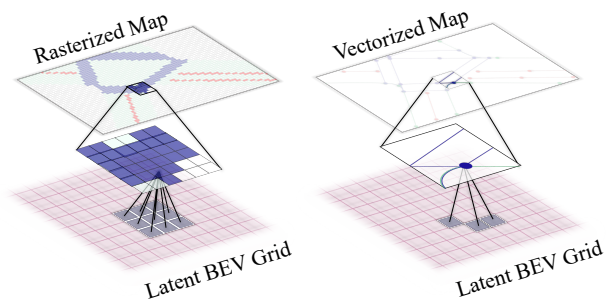


Figure 1. Schematic relation between output element and latent BEV grid. Rasterized decoding (left) and vectorized decoding (right) provide dense and sparse spatial supervision, respectively.

isions. Typically, a High-Definition (HD) map is given *a priori* to capture essential information such as lanes, dividers, crosswalks, and other static elements. However, the real world is subject to change due to events such as construction, road closures, or weather conditions. Hence, the construction of online maps from the perception system is essential to ensure safety.

An online HD map informs the autonomous vehicle about its environment in real time. Maps represent characteristics of the traffic scene, where its static elements may not be fully defined, *e.g.*, defining lanes purely based on the visible markings might fail in case of their absence. Hence, characteristics of the traffic scene must be derived from the infrastructure context, which requires a holistic semantic understanding of the traffic scene. In the case of lanes, other infrastructure elements, such as curbs, must be considered. Furthermore, most autonomous vehicle systems require the vectorized map for use in their planning systems, as it is computationally efficient and avoids ambiguity [7, 19, 21].

Related works for online HD map construction commonly perform pixel-level semantic segmentation in a 2D top-down view to predict a Bird’s-Eye View (BEV) raster map [15, 29, 32]. A vectorized representation can be derived from this intermediate raster map representation in a post-processing step [14]. Recent approaches [19, 21, 42]

introduce vector map decoding to predict the spatial position of static elements with polylines and thus directly generate the vectorized representation of the target.

Both paradigms leverage the same learned BEV encoder concept that fuses data from multiple sensors into one joint latent BEV feature grid [32], or BEV grid for shorthand, which is a spatial grid representation of the environment encoded in the latent feature space. However, as shown in Fig. 1, rasterized map decoders (left) and vectorized map decoders (right) have different extents of spatial supervision. First, raster map decoders predict pixel-level classifications. Outputs and labels are both dense rasters, providing a dense pixel-wise loss for optimization. In contrast, vector decoders have sparse outputs and labels, resulting in reduced guidance from the sparse loss.

Secondly, raster map decoders typically use convolutional layers, where each cell in the latent BEV grid contributes to the output. In contrast, vector map decoders typically use deformable attention-based mechanisms, such as deformable DETR [47], where only a subset of latent BEV grid cells contributes to the output. Therefore, in a single training step, a raster map decoder optimizes all cells of latent BEV grid (dense spatial supervision), while vector map decoder optimizes only a subset (sparse supervision).

Based on this reasoning, we argue that including dense spatial supervision provides additional guidance for deriving the high-quality vectorized HD map. A common approach is adding an auxiliary semantic segmentation task [6, 13, 19]. We propose a novel latent BEV feature grid augmentation method that directly injects dense spatial features from an intermediate predicted raster map into the latent BEV grid. We further incorporate gradient stopping to treat the predicted raster map as an immutable prior. To verify our method, we implement AugMapNet, a model that leverages latent BEV grid processing and augmentation to improve the performance of vector map decoders.

In summary, the main contributions of this paper are:

- We propose a latent BEV grid augmentation method that combines vector decoding and dense spatial supervision.
- We develop a new model, AugMapNet, that adds latent augmentation for dense spatial supervision, along with gradient stopping and extra BEV processing, and demonstrate its effectiveness through extensive experiments.
- We show that applying our method significantly enhances the structure in the latent BEV grid, which correlates with improved vector map decoding performance.

2. Related Work

2.1. Rasterized Map Construction

One option to represent map elements is a rasterized form (Fig. 1, left). Philion and Fidler [32] proposed the first learning-based architecture for online raster map construc-

tion from camera images by performing pixel-wise classification. BEVFormer [15] and subsequent works, including BEVFormer v2 [41], BEVDet4D [10], VideoBEV [8], StreamPETR [38], SoloFusion [30], and TempBEV [26], improve accuracy by aggregating temporal information across multiple time steps. Like previous approaches, HDMapNet [14] performs semantic segmentation first, but adds a post-processing step to derive a vectorized representation. While raster map prediction leads to dense spatial supervision, post-processing is required to get a vectorized form [19, 21], which is typically based on heuristics and restricts scalability and performance [14, 21]. In AugMapNet, we directly predict vectorized representations and still utilize dense spatial supervision by using our method.

2.2. Vectorized Map Construction

Recent approaches directly predict the vectorized representation of map elements. Early works focus on topology and limit themselves to only lane centerlines [2, 24, 48]. VectorMapNet [21] was the first end-to-end model to showcase the benefit of directly predicting a vectorized map representation including drivable areas, boundaries, dividers, and crosswalks. MapTR [19] addresses the ambiguity in selecting a discrete set of points to model geometries in vectorized representations by employing permutation-equivalent modeling, which stabilizes the learning process. StreamMapNet [42] uses memory buffers to achieve temporal stability, aiding in the construction of local HD maps.

All recent vector map decoders [19, 21, 27, 42] share the same underlying deformable DETR [47] mechanism for decoding (see Fig. 1, right). Its deformable attention mechanism samples K keys as a subset of all the latent BEV grid feature vectors. Only a subset of the BEV grid cells contributes to the sparse vectorized output, leading to sparse spatial supervision. Hence, this type of vector map decoder is expected to exhibit a latent space with less spatial structure compared to raster map decoders. In AugMapNet, we extend this type of existing models with a novel latent BEV grid augmentation method to combine the benefits of direct vectorized prediction and dense spatial supervision.

2.3. Prior and Topology-Aware Map Methods

External prior maps can enhance online HD map construction, a concept explored by works like P-MapNet [11], SMERF [22], and NavMapFusion [28]. These methods leverage readily available Standard-Definition maps to improve performance, particularly at longer ranges. In addition, SMERF and Chameleon [45] predict complex topological structures, such as intersections and virtual lanes, usually overlooked by standard pipelines. While these approaches rely on external prior data, our BEV grid augmentation is an orthogonal, prior-less method that uses a self-generated “prior” to enhance HD map construction.

2.4. Latent Space Supervision and Analysis

A straightforward approach to add spatial supervision is adding an auxiliary semantic segmentation task, as done by PivotNet [6], MapTRv2 [19], and SeaBird [13]. MapVR [43] adds a differentiable rasterizer on top of a vector map decoder only for training. A downstream auxiliary segmentation loss provides supervision directly to the vectorized output. We extend their argument that more sophisticated techniques can increase performance beyond pure auxiliary supervision [43] by introducing the AugMapNet approach, where the segmentation loss does not backpropagate to the latent BEV grid and is therefore not an auxiliary loss.

Two recent works also leverage a raster representation beyond auxiliary supervision. HIMap [46] introduces a hybrid representation that jointly decodes both raster and vector outputs. In contrast, we adopt a two-stage approach in which raster decoding preconditions subsequent vector decoding. MGMap [20] likewise employs a two-stage strategy, generating an intermediate rasterized representation from which the vectorized map is predicted. However, in two-stage designs, the raster output can become a high-frequency latent space [5]. To address this, we apply gradient stopping to treat the intermediate representation as an independent prior. In summary, our mechanism combines raster and vector representations better than other hybrid architectures, while being modular enough to be easily transferred to different models. It augments the latent BEV space and preconditions the vector map decoding, which adds more structure to the final latent BEV grid.

We support our claims via analysis and visualizations on the latent BEV grid features with PCA [9]. Since our evaluation already demonstrates that learning a non-linear decoder on these latent features results in superior metric scores, we opt for the simplicity of PCA instead of non-linear approaches, such as t-SNE [37] and UMAP [23].

Other works in related tasks leverage latent BEV grid visualizations, but often do not analyze the latent BEV grid for further insights into their mechanisms. SA-BEV [44], which proposes a pooling mechanism to improve the semantics of the latent BEV grid features, and BEV-SAN [3], which adds height slices to the BEV grid, only visualize each cell’s feature vector norm to produce a grayscale image without additional quantitative analysis. FB-BEV [16] uses RGB BEV feature visualizations to support its claims, but lacks details on how BEV features are reduced to RGB and also lacks analysis of the BEV features.

Instead of cameras, some works that visualize and analyze latent features use LiDAR input. Range image visualizations rely on t-SNE in RangeRCNN [17], whereas others [31, 35] use t-SNE to show class-colored latent features that form distinct clusters. Perez *et al.* [31] analyze their BEV features via the average relative distances between classes, whereas we use the mean Silhouette score [34].

3. Approach

3.1. Problem Statement

Let $U = \{u_1, \dots, u_n\}$ be the set of image frames from the n monocular cameras mounted on the autonomous vehicle. Let $\mathcal{M}_{\text{vector}} = \{P_{\text{div}}, P_{\text{bound}}, P_{\text{ped}}\}$ be the local HD map with the autonomous vehicle at the origin, where P_{div} , P_{bound} , and P_{ped} are the sets of polylines representing lane dividers, road boundaries, and pedestrian crossings within the scene, respectively. Each polyline $P_k = [(x_i, y_i)]_{i=1}^{N_{P_k}}$ is a sequence of N_{P_k} points. The goal is to find a function f that predicts the local vectorized HD map $\hat{\mathcal{M}}_{\text{vector}}$ from the set of image frames U , *i.e.*, $\hat{\mathcal{M}}_{\text{vector}} = f(U)$. The function f is typically realized in an encoder-decoder fashion [14, 19, 21, 42]. An encoder e_{BEV} generates the latent BEV grid B , *i.e.*, $B = e_{\text{BEV}}(U)$. A decoder d_{vector} performs vector decoding into the local HD map representation, *i.e.*, $\hat{\mathcal{M}}_{\text{vector}} = d_{\text{vector}}(B)$.

3.2. Latent BEV Grid Augmentation

First, we provide a mathematical framework for the terms “dense” and “sparse” spatial supervision. Generally, the loss is calculated over all elements of the output representation $\hat{\mathcal{M}}$. Supervision for a step is done by optimizing learnable weights W based on the gradients of the loss: $\frac{\partial L}{\partial W} = \frac{\partial L}{\partial \hat{\mathcal{M}}} \frac{\partial \hat{\mathcal{M}}}{\partial W}$. The total amount of spatial supervision therefore is related to the number of elements in $\hat{\mathcal{M}}$. In the case of a raster map decoder, the total gradient signal is calculated from the dense loss over all cells of the raster map ($\mathbb{R}^{H \times W}$), which gives the total number of elements $|\hat{\mathcal{M}}_{\text{raster}}| = H \cdot W$. In the case of a vector map decoder, the total gradient signal is calculated from the sparse loss over N_p points of N polylines. The number of elements providing supervision is at most $|\hat{\mathcal{M}}_{\text{vector}}| = N \cdot N_p$. In typical settings, such as AugMapNet, this inequality on cardinality generally holds: $|\hat{\mathcal{M}}_{\text{raster}}| > |\hat{\mathcal{M}}_{\text{vector}}|$. This quantifies the benefit of dense spatial supervision (see more details in Supplementary B). Note that, in DETR-style decoders, out of N predicted elements, the ones correctly predicted as empty class do not induce spatial supervision. Hence, this number is the upper bound and the actual supervision is typically much sparser in a single step.

Given this motivation for dense spatial supervision, the goal is to combine rasterized prediction with decoding a vector map representation. To this end, we propose a novel concept of augmenting the latent BEV grid B with additional information from a predicted raster map. During training, we rasterize the ground truth $\mathcal{M}_{\text{vector}}$ into $\mathcal{M}_{\text{raster}}$ and train a parallel raster map decoder to predict $\hat{\mathcal{M}}_{\text{raster}}$. Given an encoder e_{raster} that preserves the spatial structure, the BEV augmentation mechanism is defined as:

$$B_{\text{aug}} = B + e_{\text{raster}}(\hat{\mathcal{M}}_{\text{raster}}). \quad (1)$$

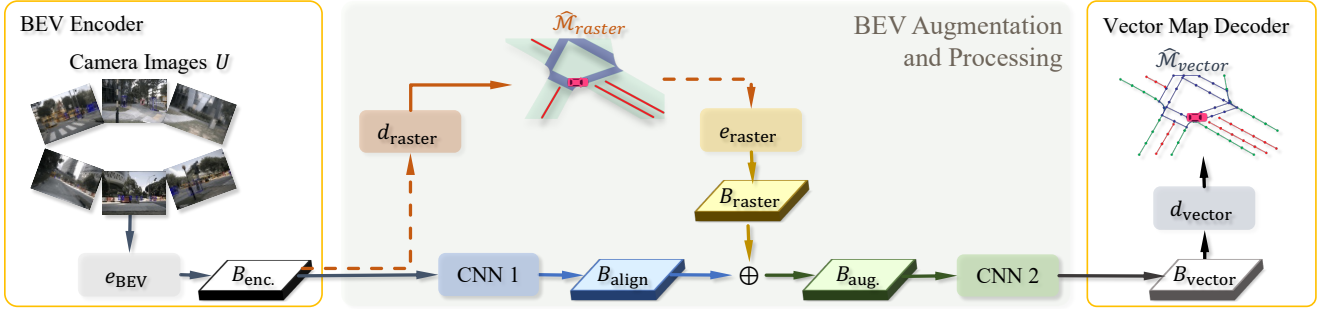


Figure 2. Overview of AugMapNet architecture. Camera images U are processed by learned BEV encoder e_{BEV} into latent BEV grid B_{enc} . AugMapNet employs a latent BEV grid augmentation mechanism that generates \hat{M}_{raster} (*i.e.*, map semantic segmentation). Additional CNNs help structure the latent space. A vector map decoder d_{vector} predicts vectorized map \hat{M}_{vector} . Dashed lines indicate gradient stop.

By injecting the spatial features into the latent BEV grid, we expect to enhance its spatial structure. Directly adding the encoded spatial features is expected to have a stronger impact than auxiliary supervision. B_{aug} is then used instead of B in the vector map decoder to produce the final prediction.

3.3. AugMapNet Model Architecture

We design a novel model, AugMapNet, to demonstrate the benefit of our proposed latent BEV grid augmentation concept. The full architecture is shown in Fig. 2. On a high level, AugMapNet extends any given encoder-decoder structure with e_{BEV} and d_{vector} with a BEV space augmentation. AugMapNet uses a learned BEV encoder e_{BEV} to encode given camera images U into the BEV grid B_{enc} . We add a parallel rasterized map decoder d_{raster} that predicts the rasterized map \hat{M}_{raster} from B_{enc} . Following the BEV augmentation concept from Eq. (1), \hat{M}_{raster} is encoded by e_{raster} and added back to the latent BEV grid B_{enc} , resulting in the augmented BEV grid B_{aug} . We introduce additional BEV processing with 2 CNN blocks to better leverage the latent BEV grid. CNN1 transforms B_{enc} into an aligned BEV grid, B_{align} , before it is augmented by B_{raster} . CNN2 operates on B_{aug} to combine the summed features into new latent space features in B_{align} . The benefit of these CNNs is demonstrated in Sec. 4.7, where ablations are done without the CNNs. The final latent BEV grid representation, B_{vector} , is passed to the vector map decoder d_{vector} to extract the vectorized map representation \hat{M}_{vector} , comprising polylines \hat{P}_{div} , \hat{P}_{bound} , and \hat{P}_{ped} .

3.4. Loss and Gradient Stopping

The vector map decoder loss ($\mathcal{L}_{\text{vector}}$) is the same as in StreamMapNet [42] and consists of a polyline matching loss ($\mathcal{L}_{\text{line}}$), a focal loss ($\mathcal{L}_{\text{focal}}$), and a transformation loss ($\mathcal{L}_{\text{trans}}$). For the raster map decoder loss ($\mathcal{L}_{\text{raster}}$), we evaluate semantic segmentation using the Dice loss [25]. Supplementary C has the mathematical definition of all losses.

Optimizing a parallel raster representation similar to

MGMap [20] poses the risk of creating a high-frequency latent space due to the superimposed vector map decoder loss, which can hinder interpretability (*cf.* [5]). To mitigate this issue, our latent BEV grid augmentation mechanism utilizes gradient stopping, as illustrated by the dashed lines in Fig. 2. This way, the vector decoding task is decoupled from the semantic segmentation task. Specifically, gradients are not backpropagated from d_{raster} to e_{BEV} to ensure that the semantic segmentation task does not affect the latent BEV grid B_{enc} and hence does not compromise the vector map decoding performance. Furthermore, gradients are not backpropagated from e_{raster} to d_{raster} to avoid d_{raster} using the rasterized map prediction \hat{M}_{raster} as a high-frequency latent space for vector map features. The vector decoder treats the predicted rasterized map as an immutable prior and e_{raster} learns how to generate features that are useful for the vector map decoding task. Different variations of gradient stopping are evaluated in Sec. 4.7.

3.5. Structure of Latent BEV Grid

We hypothesize that our latent BEV augmentation induces a more structured latent space due to dense spatial supervision. To measure the structure, we first use cluster analysis on the latent BEV grid on which d_{vector} operates (*i.e.*, B_{vector}). Class indices from the ground truth rasterized map are used as cluster labels for each of the latent vectors (*i.e.*, each BEV grid cell). The Silhouette score [34] is used to quantify cluster cohesion and separation for cluster quality evaluation and we use its mean of all data points:

$$S = \frac{1}{N} \sum_{i=1}^N \frac{b(i) - a(i)}{\max(a(i), b(i))}, \quad (2)$$

where $a(i)$ is the average distance between i and all other points in its cluster and $b(i)$ is the minimum average distance from i to the nearest cluster that i is not a part of.

Secondly, we leverage a dimensionality reduction technique that linearly transforms the high-dimensional latent

space into a low-dimensional space that can be visualized and studied. Specifically, we perform a Principal Component Analysis (PCA) [9] on each scene’s latent features and analyze the top 3 components ordered by the amount of variance they capture from the data. We quantify the similarity between GT label and latent BEV grid for each scene by measuring the Mutual Information [36] between the ground truth (GT) raster map $\mathcal{M}_{\text{raster}}$ and the top 3 principal components of B_{vector} . Formally, given two sets of labels U and V , Mutual Information is defined as :

$$MI(U, V) = \sum_{i=1}^{|U|} \sum_{j=1}^{|V|} \frac{|U_i \cap V_j|}{N} \log \left(\frac{N|U_i \cap V_j|}{|U_i||V_j|} \right). \quad (3)$$

In our case, U represents the flattened ground truth raster map after representing each cell with a unique class index. Following common practice for mutual information estimation [12], we partition the continuous space of the PCA result into bins of finite size and choose 10 equidistant bins per dimension. V represents the flattened PCA result after binning and mapping each cell to a unique index.

4. Experiments

4.1. Datasets and Evaluation Metrics

We conduct our experiments on nuScenes [1], which provides samples at 2Hz, and Argoverse2 [40], which we resample to 2Hz for consistency. We use images from the 6 (nuScenes) or 7 (Argoverse2) monocular cameras and corresponding ground truth vectorized map elements: road boundary (bound), lane dividers (div), and pedestrian crossings (ped). We use StreamMapNet’s [42] train and validation splits with no geospatial overlap for evaluation.

The performance on the vector map decoding task is evaluated for each of the three classes of polylines using Average Precision (AP) and combined with mean Average Precision (mAP). Following StreamMapNet, the AP thresholds are $\{0.5, 1.0, 1.5\}$ and $\{1.0, 1.5, 2.0\}$ for the $60\text{ m} \times 30\text{ m}$ and $100\text{ m} \times 50\text{ m}$ perception ranges, respectively. Intersection over Union (IoU) is evaluated per class for the raster map decoding task and reported as mean IoU (mIoU). The model runtime is evaluated in frames per second (FPS).

4.2. Baseline Models

We use several state-of-the-art models for vectorized map prediction as baselines: MapTR [19], P-MapNet [11], SQD-MapNet [39], and StreamMapNet [42]. Additionally, we compare against hybrid methods that combine raster and vector representations: MapTRv2 [19], MapVR [43], and MGMap [20]. For a fair and direct comparison, we ran all baselines on nuScenes and method-specific baselines on Argoverse2 ourselves and used the settings from StreamMapNet and SQD-MapNet for training AugMapNet and AugMapNet-SQD (AugSQD for short), respectively.

4.3. Implementation Details

StreamMapNet [42] is our baseline implementation with BEVFormer [15] as the BEV encoder e_{BEV} and temporal aggregation is done with a Gated Recurrent Unit (GRU) [4]. The vector map decoder d_{vector} is the custom deformable DETR decoder [47] from StreamMapNet [42] that uses Multi-Point Attention.

We perform semantic segmentation on the three classes: lane dividers, road boundaries, and pedestrian crossings. Thus, $\hat{\mathcal{M}}_{\text{raster}} \in \mathbb{R}^{100 \times 50 \times 3}$. The decoder d_{raster} is a 4-layer CNN with output channels $\{128, 64, 32, 3\}$. The encoder e_{raster} is a 4-layer CNN with output channels $\{32, 64, 128, 256\}$. CNN1 and CNN2 both have 2 layers with input and output channel sizes of 256. All CNNs use convolutions with kernel size 3 and stride 1, batch normalization, and ReLU. With this configuration, AugMapNet has 52.70 million parameters, 6.3 % more than StreamMapNet. We train the model for 24 epochs using a batch size of 1, with the training performed in parallel on 8 Nvidia V100 GPUs. AdamW optimizer is used with cosine annealing and a 2.5×10^{-4} learning rate.

4.4. Quantitative Results

Tab. 1 shows the results of our AugMapNet model in comparison to relevant baseline models on the nuScenes dataset. Naive auxiliary semantic segmentation (+Aux.) by adding d_{raster} optimized with $\mathcal{L}_{\text{raster}}$ gives a slight improvement with 34.0 % mAP. The results show that AugMapNet outperforms all baselines on the overall mAP, and on each class-specific metric except for P-MapNet on AP_{bound} due to its map prior. Overall, AugMapNet achieves 38.3 % mAP vs. 33.8 % mAP for StreamMapNet. This translates to 13.3 % relative improvement over the state-of-the-art StreamMapNet model. While the relative improvements on lane dividers (11.0 %) and road boundaries (5.6 %) are strong, the relative improvement on pedestrian crossings is immense (26.3 %). The FPS of AugMapNet differs only slightly from StreamMapNet with a relative change of -9.6% . The model size also remains almost the same at 1.8 GB for both StreamMapNet and AugMapNet. During training with batch size 1, we observe ≈ 7.7 GB VRAM usage, a 1.6 % increase over StreamMapNet. More details are given in Supplementary E.

Tab. 3 shows results on a larger perception range and on applying our method to a different model. Beyond the reported 13.3 % improvement on 60 m, we get 24.6 % on 100 m. We provide further ablation on perception ranges in Supplementary A, showing an increase in relative improvement at larger perception ranges. To verify generalizability of our method, we apply our proposed latent BEV augmentation method to another model, SQD-MapNet [39], and denote it as AugSQD. The improvement is 9.8 % on perception range 60 m and 21.1 % on the 100 m range.

Method	AP _{ped}	AP _{div}	AP _{bound}	mAP	FPS
MapTR [18]	7.5	23.0	35.8	22.1	16.0
MapVR [†] [43]	10.1	22.6	35.7	22.8	16.0
MGMap [†] [20]	7.9	25.6	37.4	23.7	11.8
MapTRv2 [†] [19]	16.2	28.7	44.8	29.9	14.9
P-MapNet [†] [11]	17.7	26.1	48.4	30.7	12.2
SQD-MapNet [39]	34.8	31.7	44.3	36.9	11.9
StreamMapNet [42]	31.2	27.3	42.9	33.8	13.2
StreamMapNet + Aux. [†]	31.9	27.7	42.3	34.0	13.2
AugMapNet [†] (ours)	39.4	30.3	45.3	38.3	11.9
AugSQD [†] (ours)	41.1	32.6	47.8	40.5	10.8

Table 1. AugMapNet compared to baselines at perception range 60 m × 30 m on nuScenes split without geospatial overlap [33]. “AugSQD” is the application of our method to SQD-MapNet [39]. * denote the use of prior map, results from [11]. [†] denotes hybrid architectures. “Aux.” is auxiliary segmentation (see Section 4.4).

Method	AP _{ped}	AP _{div}	AP _{bound}	mAP	FPS
VectorMapNet [21]	35.6	34.9	37.8	36.1	5.5
MapTR [18]	48.1	50.4	55.0	51.1	18.0
StreamMapNet [42]	56.0	54.4	61.0	57.1	14.2
AugMapNet (ours)	57.4	57.4	61.6	58.8	12.8

Table 2. Performance on Argoverse2. Baseline results from [42].

To assess the generalization of our method across datasets and sensor configurations, we trained AugMapNet on Argoverse2 dataset [40] without any adjustments. Argoverse2 covers different cities and a different sensor configuration (7 vs. 6 cameras). Tab. 2 shows the results of our AugMapNet model in comparison to relevant baseline models. Again, AugMapNet outperforms all other approaches and reaches 58.8% mAP, a significant improvement over StreamMapNet, confirming the broader applicability of our method. Results on Argoverse2 for larger perception ranges and AugSQD are given in Supplementary G.

4.5. Qualitative Results

Fig. 3 shows qualitative results of StreamMapNet and AugMapNet on a traffic scene from the nuScenes dataset. Both models correctly predict the lane dividers and road boundaries. AugMapNet detects the crosswalk in front of the autonomous vehicle that is missed by StreamMapNet, which exemplifies our large gains on pedestrian crossings. More examples can be found in the Supplementary I.

4.6. Results on Latent BEV Grid Analysis

We compare the latent BEV grid features of StreamMapNet and AugMapNet with respect to: 1) cluster analysis, 2) similarity to GT label, 3) variance. First, we use cluster analysis on the latent BEV grid input to d_{vector} (i.e., B_{vector} in AugMapNet) to verify our hypothesis that latent BEV grid augmentation increases structure of the latent BEV grid. For scene 2 in Fig. 4, AugMapNet reaches a Silhouette score of 0.119 vs. 0.086 for StreamMapNet. Over the full nuScenes val dataset, the mean Silhouette score

Range	Variant	AP _{ped}	AP _{div}	AP _{bound}	mAP	Impr.
60 m × 30 m [‡]	StreamMapNet [42]	31.2	27.3	42.9	33.8	13.3 %
	AugMapNet (ours)	39.4	30.3	45.3	38.3	
100 m × 50 m [*]	StreamMapNet [42]	25.5	19.3	24.7	23.2	24.6 %
	AugMapNet (ours)	35.5	22.8	28.4	28.9	
60 m × 30 m [‡]	SQD-MapNet [39]	34.8	31.7	44.3	36.9	9.8 %
	AugSQD (ours)	41.1	32.6	47.8	40.5	
100 m × 50 m [*]	SQD-MapNet [39]	26.9	20.9	27.6	25.1	21.1 %
	AugSQD (ours)	33.0	24.7	33.6	30.4	

Table 3. Results on different perception ranges for AugMapNet and AugSQD. Results on nuScenes [1]. AP thresholds [‡]: {0.5, 1.0, 1.5}, ^{*}: {1.0, 1.5, 2.0}.

for AugMapNet is 4.5 times higher than StreamMapNet (0.076 vs. 0.017). Therefore, features from the BEV grid of the same class are better clustered in the latent space of AugMapNet compared to StreamMapNet, which could benefit classification. Since the ground truth labels have spatial structure, feature consistency among neighboring cells will also give a more consistent signal to the decoder.

Secondly, to assess the similarity between GT label and latent BEV grid, we perform a PCA for each latent space and visualize the top 3 principal components ordered by the amount of captured variance for StreamMapNet and AugMapNet on two nuScenes data points in Fig. 4 (more results are in Supplementary J). The results show spatial similarity with both the vectorized and rasterized map ground truths. Areas like background and drivable roads are well segmented and retrievable from the principal components. In both scenes, similarity appears higher for AugMapNet, which matches the cluster analysis results. AugMapNet results also have sharper boundaries that align well with the GT. To quantify the similarity, we compare Mutual Information (MI) values. In scene 2 in Fig. 4, StreamMapNet has an MI of 0.721, while AugMapNet has 0.761 (+5.5%), which aligns with higher visual similarity. For the whole nuScenes dataset, the latent BEV grid of StreamMapNet has an MI of 0.61 ± 0.09 , while AugMapNet has 0.64 ± 0.09 (+4.9%). To show that higher similarity is related to improved vector map prediction performance, we plot the mAP over MI for all nuScenes val data points in Fig. 5a (note: data points with 0.67 mAP are mostly scenes where the model predicts nonexistent crosswalks). We measure a positive linear correlation between MI and vector map prediction performance, with $R^2 = 0.12$ for StreamMapNet and $R^2 = 0.22$ for AugMapNet. To determine whether AugMapNet’s increase of MI is statistically significant, we conduct a one-tailed t-test at a significance level $\alpha = 0.01$. The test yields $p \ll 0.001$, thus, we reject the null hypothesis and conclude that MI is significantly higher in AugMapNet. This result, in combination with the observed positive correlation between MI and vector map prediction performance, gives an interpretable insight and intuitive understanding of the performance improvement of AugMapNet.

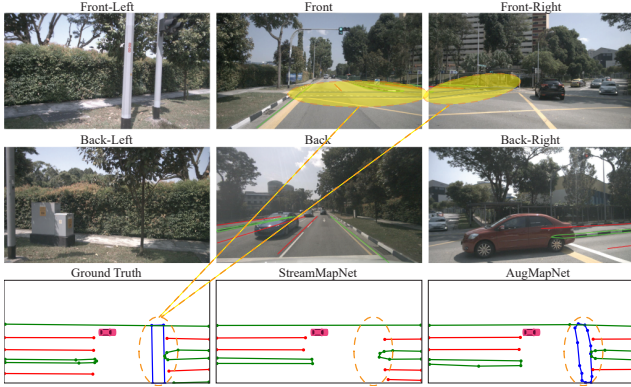


Figure 3. Qualitative result on nuScenes dataset. Input camera images (U) are at the top. Ground truth labels ($\mathcal{M}_{\text{vector}}$) and predicted vectorized maps ($\hat{\mathcal{M}}_{\text{vector}}$) are at the bottom. The orange circle highlights the crosswalk missed by StreamMapNet.

Thirdly, a more structured latent BEV grid is expected to have an effect on its variance. We calculate the spatial variance of each channel in the latent BEV grids and take an average across all channels. For example, in scene 2 in Fig. 4, the variance of StreamMapNet latent space is 0.103 vs. 0.068 for AugMapNet. Results on the full nuScenes val dataset indicate that the latent space of AugMapNet indeed has a significantly lower variance (0.055 ± 0.006) compared to StreamMapNet (0.087 ± 0.008). We assume the variance reduction is caused by the BEV augmentation in AugMapNet. The raster map predicted in the BEV augmentation branch only carries low-dimensional class information due to the gradient stop from e_{raster} to $\hat{\mathcal{M}}_{\text{raster}}$. Mapping this low-dimensional signal into the high-dimensional BEV grid latent space is expected to have a governing effect and reduce spatial variance. An analysis of the relation between spatial variance of the latent BEV grid and vector map prediction performance is shown in Fig. 5b. In StreamMapNet, the variance does not correlate with prediction performance ($R^2 = 0.002$). In contrast, AugMapNet shows a positive correlation ($R^2 = 0.143$), suggesting that its spatial variance is explained by relevant, task-specific features.

4.7. Ablation of Latent BEV Grid Augmentation

We evaluate our proposed latent BEV grid augmentation method and compare different variants of gradient stopping. To allow a direct comparison with StreamMapNet, we do not include the additional processing CNNs (*i.e.*, CNN1 and CNN2 in Fig. 2). The results on the nuScenes dataset are shown in Tab. 4. The baseline is StreamMapNet with 33.8% mAP. First, we run an Oracle experiment to determine the upper bound of our BEV augmentation mechanism. Here, the GT raster map, $\mathcal{M}_{\text{raster}}$, not the predicted raster map, $\hat{\mathcal{M}}_{\text{raster}}$, is passed to e_{raster} ; hence, the IoU scores are 100.0%. It achieves 91.4% mAP, confirming our method’s potential to improve vector map decoding.

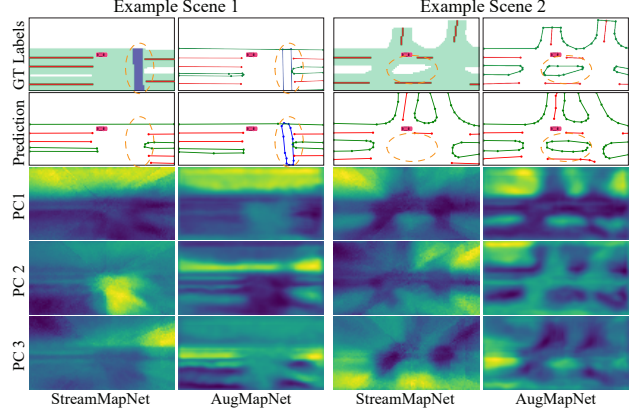


Figure 4. Rendering of GT $\mathcal{M}_{\text{raster}}$ and $\mathcal{M}_{\text{vector}}$, prediction $\hat{\mathcal{M}}_{\text{vector}}$, and the top 3 principal components of the latent BEV grid input to d_{vector} for StreamMapNet and AugMapNet (PC1-3). Orange circles highlight elements missed by StreamMapNet.

Variant	∇d	∇e	AP _{ped}	AP _{div}	AP _{bound}	mAP	mIoU
Baseline	-	-	32.4	28.8	42.5	33.8	-
Oracle	-	-	88.4	96.6	89.0	91.4	100.0
Full backprop	✓	✓	32.9	29.3	42.3	34.8	41.4
d_{raster} grad stop	✗	✓	30.8	28.1	41.5	33.5	27.3
e_{raster} grad stop	✓	✗	33.3	29.1	42.7	35.0	43.6
Isolated	✗	✗	33.9	29.9	42.7	35.5	28.5

Table 4. Ablation of BEV augmentation on nuScenes. Oracle uses GT, $\mathcal{M}_{\text{raster}}$, for augmentation. ∇ indicates whether gradients are backpropagated from either d_{raster} or e_{raster} (*i.e.*, dashed lines in Fig. 2). AP and mIoU evaluate $\hat{\mathcal{M}}_{\text{vector}}$ and $\hat{\mathcal{M}}_{\text{raster}}$, respectively.

The BEV augmentation mechanism introduces d_{raster} to decode $\hat{\mathcal{M}}_{\text{raster}}$ from B_{enc} and e_{raster} to encode it to B_{raster} . With no gradient stopping (“Full backprop”), it gives a small improvement with 34.8% mAP. This variant also does raster map decoding well with 41.4% mIoU.

Stopping the backpropagation between d_{raster} and e_{BEV} (“ d_{raster} grad stop”) slightly drops vector map decoding performance to 33.5% mAP. This is expected, since d_{raster} is optimized by both $\mathcal{L}_{\text{vector}}$ and $\mathcal{L}_{\text{raster}}$, but has no influence on its input B_{enc} . As a result, a high-frequency latent space is likely formed by backpropagation. A comparison with the “Isolated” case (see below) shows that this hurts performance. Surprisingly, the raster map decoder still achieves 27.3% mIoU from a latent BEV grid that was only optimized for the vector map decoding task. This finding suggests that decoding raster and vector representations requires similar latent features and that a hybrid approach can conceptualize abstract features useful for decoding both representations of the same underlying map information.

Alternatively, stopping the backpropagation from e_{raster} to d_{raster} (“ e_{raster} grad stop”) improves performance to 35.0% mAP and 43.6% mIoU. Finally, stopping backpropagation at both locations (“Isolated”) achieves the best result with 35.5% mAP. “Isolated” is used in AugMapNet,

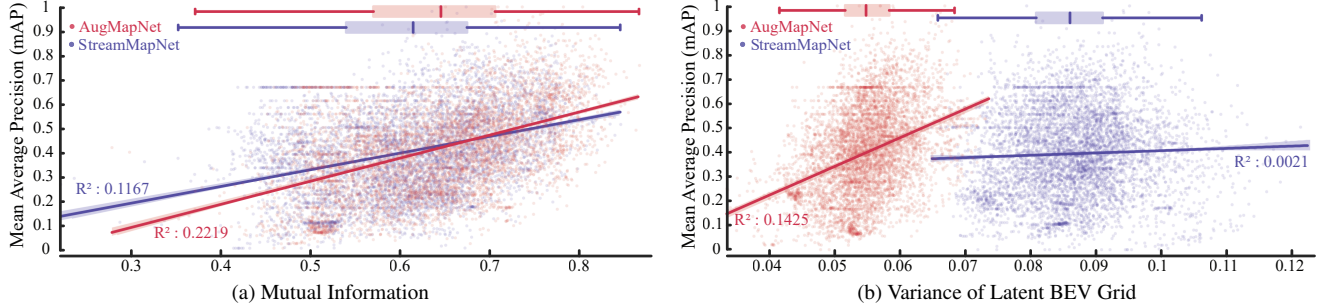


Figure 5. Vectorized map prediction performance versus (a) Mutual Information between top 3 principal components and ground truth raster map and (b) Variance of latent BEV grid for all nuScenes val data points. (StreamMapNet: blue, AugMapNet: red)

Index	# Layers	AP _{ped}	AP _{div}	AP _{bound}	mAP
a)	0	31.2	27.3	42.9	33.8
b)	1	36.4	30.0	43.7	36.7
c)	2	38.9	29.6	43.5	37.3
d)	3	36.7	30.0	43.1	36.6
e)	4	34.3	30.0	44.8	36.4

Table 5. Ablation of number of layers for BEV processing CNNs. a) is StreamMapNet [42] and e) is AugMapNet’s setting.

since it cuts off the rasterized map branch from the rest of the model. Specifically, the latent BEV grid before augmentation, B_{align} , is unaffected by the segmentation loss and can purely optimize for vector map decoding. \hat{M}_{raster} is learned separately and augments the latent BEV grid to improve the features for vector map decoding. Supplementary D provides a theoretical foundation for the empirical results of gradient stopping discussed in this section.

4.8. Ablation of Latent BEV Grid Processing

This study, shown in Tab. 5, compares different variants for additional processing between the encoder and decoder. Here we do not use our BEV augmentation to allow direct comparison with the StreamMapNet baseline, thus there is only one CNN block (*i.e.*, CNN1 in Fig. 2). Comparing StreamMapNet (a) with index (b) shows that we get a significant improvement of 8.6 % mAP just from adding a single convolution layer. Another layer (c) gives a slight improvement, but further layers show a performance plateau (d, e). Thus we choose 2 CNN layers (c) for AugMapNet. Ablation on the kernel size is provided in Supplementary H.

4.9. Ablation of Key Components of AugMapNet

We assess the performance gains from AugMapNet’s two key components: (1) latent BEV grid processing and (2) latent BEV grid augmentation. As seen in Tab. 6, BEV processing improves the StreamMapNet baseline by 8.6 %. In Tab. 5, we saw that gains saturated at two CNN layers, with more layers adversely affecting results. Despite this, our augmentation mechanism, which has 4 layers split across 2 CNN blocks, provides an additional 4.4 % gain, bringing

Component	60 m × 30 m	100 m × 50 m	150 m × 75 m
Baseline	33.8	23.2	6.9
+ CNNs	36.7 (+8.6%)	26.2 (+12.9%)	8.9 (+28.9%)
+ Aug	38.3 (+4.4%)	28.9 (+10.3%)	9.8 (+10.1%)

Table 6. Ablation of key components of AugMapNet on nuScenes.

the full AugMapNet model to 38.3 % mAP. This additional improvement is even stronger for challenging long-range predictions: 10.3 % on the 100 m × 50 m range and 10.1 % on the 150 m × 75 m range. These results show the distinct roles of each component: latent BEV grid processing enhances the latent features, while augmentation refines the latent grid with dense spatial information, which is critical for long-range predictions.

5. Conclusion

We presented AugMapNet, a novel method for online vectorized HD map construction from multiple camera views. It enhances the latent BEV grid by further processing the features and then injecting spatial features from a predicted raster map, thus providing better dense spatial supervision for the vector decoder than other hybrid architectures. Experiments on nuScenes and Argoverse2 show an improvement in mAP of up to 13.3 % over the StreamMapNet baseline and even higher improvements on larger perception ranges with minimal parameter overhead. AugMapNet shows particular strength in detecting complex map characteristics, such as pedestrian crossings, with a substantial 26.3 % relative performance gain.

Additionally, our analysis of the latent BEV grid reveals that AugMapNet forms a more structured and task-relevant feature space. Mutual Information analysis shows that AugMapNet’s augmented BEV grid has much higher similarity with the ground truth raster map, which is correlated with improved vector map predictions.

In conclusion, AugMapNet highlights the importance of dense spatial supervision in BEV-based vector map construction and provides an effective method to improve the latent structure generated by learned BEV encoders.

References

- [1] Holger Caesar, Varun Bankiti, Alex H Lang, Sourabh Vora, Venice Erin Liong, Qiang Xu, Anush Krishnan, Yu Pan, Giancarlo Baldan, and Oscar Beijbom. nuscenes: A multimodal dataset for autonomous driving. In *CVPR*, pages 11621–11631, 2020. 5, 6, 11, 12, 13
- [2] Yigit Baran Can, Alexander Liniger, Danda Pani Paudel, and Luc Van Gool. Structured bird’s-eye-view traffic scene understanding from onboard images. In *ICCV*, pages 15661–15670, 2021. 2
- [3] Xiaowei Chi, Jiaming Liu, Ming Lu, Rongyu Zhang, Zhaoqing Wang, Yandong Guo, and Shanghang Zhang. Bev-san: Accurate bev 3d object detection via slice attention networks. In *CVPR*, pages 17461–17470, 2023. 3
- [4] Kyunghyun Cho, Bart van Merriënboer, Caglar Gulcehre, Dzmitry Bahdanau, Fethi Bougares, Holger Schwenk, and Yoshua Bengio. Learning phrase representations using RNN encoder–decoder for statistical machine translation. In *Proceedings of the 2014 Conference on Empirical Methods in Natural Language Processing (EMNLP)*, pages 1724–1734, Doha, Qatar, 2014. Association for Computational Linguistics. 5
- [5] Casey Chu, Andrey Zhmoginov, and Mark Sandler. CycleGAN, a master of steganography. In *Machine Deception Workshop at NeurIPS*, 2017. 3, 4
- [6] Wenjie Ding, Limeng Qiao, Xi Qiu, and Chi Zhang. Pivotnet: Vectorized pivot learning for end-to-end hd map construction. In *ICCV*, pages 3672–3682, 2023. 2, 3
- [7] Jiyang Gao, Chen Sun, Hang Zhao, Yi Shen, Dragomir Anguelov, Congcong Li, and Cordelia Schmid. Vectornet: Encoding hd maps and agent dynamics from vectorized representation. In *CVPR*, pages 11525–11533, 2020. 1
- [8] Chunrui Han, Jinrong Yang, Jianjian Sun, Zheng Ge, Runpei Dong, Hongyu Zhou, Weixin Mao, Yuang Peng, and Xiangyu Zhang. Exploring recurrent long-term temporal fusion for multi-view 3d perception. *IEEE Robotics and Automation Letters*, 2024. 2
- [9] Harold Hotelling. Analysis of a complex of statistical variables into principal components. *Journal of educational psychology*, 24(6):417, 1933. 3, 5
- [10] Junjie Huang and Guan Huang. Bevdet4d: Exploit temporal cues in multi-camera 3d object detection. *arXiv preprint arXiv:2203.17054*, 2022. 2
- [11] Zhou Jiang, Zhenxin Zhu, Pengfei Li, Huan-ang Gao, Tianyuan Yuan, Yongliang Shi, Hang Zhao, and Hao Zhao. P-mapnet: Far-seeing map generator enhanced by both sdmap and hdmap priors. *IEEE Robotics and Automation Letters*, 2024. 2, 5, 6
- [12] Alexander Kraskov, Harald Stögbauer, and Peter Grassberger. Estimating mutual information. *Physical Review E—Statistical, Nonlinear, and Soft Matter Physics*, 69(6):066138, 2004. 5
- [13] Abhinav Kumar, Yuliang Guo, Xinyu Huang, Liu Ren, and Xiaoming Liu. Seabird: Segmentation in bird’s view with dice loss improves monocular 3d detection of large objects. In *CVPR*, pages 10269–10280, 2024. 2, 3
- [14] Qi Li, Yue Wang, Yilun Wang, and Hang Zhao. Hdmapnet: An online hd map construction and evaluation framework. In *2022 International Conference on Robotics and Automation (ICRA)*, pages 4628–4634. IEEE, 2022. 1, 2, 3
- [15] Zhiqi Li, Wenhai Wang, Hongyang Li, Enze Xie, Chonghao Sima, Tong Lu, Yu Qiao, and Jifeng Dai. Bevformer: Learning bird’s-eye-view representation from multi-camera images via spatiotemporal transformers. In *European conference on computer vision*, pages 1–18. Springer, 2022. 1, 2, 5
- [16] Zhiqi Li, Zhiding Yu, Wenhai Wang, Anima Anandkumar, Tong Lu, and Jose M Alvarez. Fb-bev: Bev representation from forward-backward view transformations. In *ICCV*, pages 6919–6928, 2023. 3
- [17] Zhidong Liang, Ming Zhang, Zehan Zhang, Xian Zhao, and Shiliang Pu. Rangercnn: Towards fast and accurate 3d object detection with range image representation. *arXiv preprint arXiv:2009.00206*, 2020. 3
- [18] Bencheng Liao, Shaoyu Chen, Xinggang Wang, Tianheng Cheng, Qian Zhang, Wenyu Liu, and Chang Huang. Maptr: Structured modeling and learning for online vectorized hd map construction. In *ICLR*, 2023. 6, 12
- [19] Bencheng Liao, Shaoyu Chen, Yunchi Zhang, Bo Jiang, Qian Zhang, Wenyu Liu, Chang Huang, and Xinggang Wang. Maptrv2: An end-to-end framework for online vectorized hd map construction. *International Journal of Computer Vision*, 2025. 1, 2, 3, 5, 6, 11, 12
- [20] Xiaolu Liu, Song Wang, Wentong Li, Ruizi Yang, Junbo Chen, and Jianke Zhu. Mgmmap: Mask-guided learning for online vectorized hd map construction. In *CVPR*, pages 14812–14821, 2024. 3, 4, 5, 6, 12
- [21] Yicheng Liu, Tianyuan Yuan, Yue Wang, Yilun Wang, and Hang Zhao. Vectormapnet: End-to-end vectorized hd map learning. In *International Conference on Machine Learning*, pages 22352–22369. PMLR, 2023. 1, 2, 3, 6, 12
- [22] Katie Z Luo, Xinshuo Weng, Yan Wang, Shuang Wu, Jie Li, Kilian Q Weinberger, Yue Wang, and Marco Pavone. Augmenting lane perception and topology understanding with standard definition navigation maps. In *2024 IEEE International Conference on Robotics and Automation (ICRA)*, pages 4029–4035, 2024. 2
- [23] Leland McInnes, John Healy, Nathaniel Saul, and Lukas Großberger. Umap: Uniform manifold approximation and projection. *Journal of Open Source Software*, 3(29), 2018. 3
- [24] Lu Mi, Hang Zhao, Charlie Nash, Xiaohan Jin, Jiyang Gao, Chen Sun, Cordelia Schmid, Nir Shavit, Yuning Chai, and Dragomir Anguelov. Hdmapgen: A hierarchical graph generative model of high definition maps. In *CVPR*, pages 4227–4236, 2021. 2
- [25] Fausto Milletari, Nassir Navab, and Seyed-Ahmad Ahmadi. V-net: Fully convolutional neural networks for volumetric medical image segmentation. In *2016 Fourth International Conference on 3D Vision (3DV)*, pages 565–571. Ieee, 2016. 4, 12
- [26] Thomas Monninger, Vandana Dokkadi, Md Zafar Anwar, and Steffen Staab. TempBEV: Improving learned bev encoders with combined image and bev space temporal aggreg

- gation. In *2024 IEEE/RSJ International Conference on Intelligent Robots and Systems (IROS)*, pages 9668–9675. IEEE, 2024. 2
- [27] Thomas Monninger, Zihan Zhang, Zhipeng Mo, Md Zafar Anwar, Steffen Staab, and Sihao Ding. MapDiffusion: Generative diffusion for vectorized online hd map construction and uncertainty estimation in autonomous driving. In *2025 IEEE/RSJ International Conference on Intelligent Robots and Systems (IROS)*, pages 4099–4106. IEEE, 2025. 2
- [28] Thomas Monninger, Zihan Zhang, Steffen Staab, and Sihao Ding. NavMapFusion: Diffusion-based fusion of navigation maps for online vectorized hd map construction. *arXiv preprint*, 2025. 2
- [29] Bowen Pan, Jiankai Sun, Ho Yin Tiga Leung, Alex Andonian, and Bolei Zhou. Cross-view semantic segmentation for sensing surroundings. *IEEE Robotics and Automation Letters*, 5(3):4867–4873, 2020. 1
- [30] Jinhung Park, Chenfeng Xu, Shijia Yang, Kurt Keutzer, Kris Kitani, Masayoshi Tomizuka, and Wei Zhan. Time will tell: New outlooks and a baseline for temporal multi-view 3d object detection. In *ICLR*, 2023. 2
- [31] Marc Perez, Antonio Agudo, Gijs Dubbelman, and Pavol Jancura. Class prototypical loss for enhanced feature separation in 3d object detection. In *ITSC*, 2024. 3
- [32] Jonah Philion and Sanja Fidler. Lift, splat, shoot: Encoding images from arbitrary camera rigs by implicitly unprojecting to 3d. In *Computer Vision—ECCV 2020: 16th European Conference, Glasgow, UK, August 23–28, 2020, Proceedings, Part XIV 16*, pages 194–210. Springer, 2020. 1, 2
- [33] Thomas Roddick and Roberto Cipolla. Predicting semantic map representations from images using pyramid occupancy networks. In *CVPR*, pages 11138–11147, 2020. 6
- [34] Peter J Rousseeuw. Silhouettes: a graphical aid to the interpretation and validation of cluster analysis. *Journal of computational and applied mathematics*, 20:53–65, 1987. 3, 4
- [35] Cristiano Saltori, Aljosa Osep, Elisa Ricci, and Laura Leal-Taixé. Walking your lidog: A journey through multiple domains for lidar semantic segmentation. In *ICCV*, pages 196–206, 2023. 3
- [36] Claude Elwood Shannon. A mathematical theory of communication. *The Bell system technical journal*, 27(3):379–423, 1948. 5
- [37] Laurens Van der Maaten and Geoffrey Hinton. Visualizing data using t-sne. *Journal of machine learning research*, 9(11), 2008. 3
- [38] Shihao Wang, Yingfei Liu, Tiancai Wang, Ying Li, and Xiangyu Zhang. Exploring object-centric temporal modeling for efficient multi-view 3d object detection. In *ICCV*, pages 3621–3631, 2023. 2
- [39] Shuo Wang, Fan Jia, Weixin Mao, Yingfei Liu, Yucheng Zhao, Zehui Chen, Tiancai Wang, Chi Zhang, Xiangyu Zhang, and Feng Zhao. Stream query denoising for vectorized hd-map construction. In *European Conference on Computer Vision*, pages 203–220. Springer, 2024. 5, 6, 12, 13
- [40] Benjamin Wilson, William Qi, Tanmay Agarwal, John Lambert, Jagjeet Singh, Siddhesh Khandelwal, Bowen Pan, Ratnesh Kumar, Andrew Hartnett, Jhony Kaesemodel Pontes, Deva Ramanan, Peter Carr, and James Hays. Argoverse 2: Next generation datasets for self-driving perception and forecasting. In *Proceedings of the Neural Information Processing Systems Track on Datasets and Benchmarks (NeurIPS Datasets and Benchmarks 2021)*, 2021. 5, 6, 13
- [41] Chenyu Yang, Yuntao Chen, Hao Tian, Chenxin Tao, Xizhou Zhu, Zhaoxiang Zhang, Gao Huang, Hongyang Li, Yu Qiao, Lewei Lu, et al. Bevformer v2: Adapting modern image backbones to bird’s-eye-view recognition via perspective supervision. In *CVPR*, pages 17830–17839, 2023. 2
- [42] Tianyuan Yuan, Yicheng Liu, Yue Wang, Yilun Wang, and Hang Zhao. StreamMapNet: Streaming mapping network for vectorized online hd map construction. In *WACV*, pages 7356–7365, 2024. 1, 2, 3, 4, 5, 6, 8, 11, 12, 13
- [43] Gongjie Zhang, Jiahao Lin, Shuang Wu, Zhipeng Luo, Yang Xue, Shijian Lu, Zuoguan Wang, et al. Online map vectorization for autonomous driving: A rasterization perspective. *Advances in Neural Information Processing Systems*, 36, 2023. 3, 5, 6, 12
- [44] Jinqing Zhang, Yanan Zhang, Qingjie Liu, and Yunhong Wang. Sa-bev: Generating semantic-aware bird’s-eye-view feature for multi-view 3d object detection. In *ICCV*, pages 3348–3357, 2023. 3
- [45] Zongzheng Zhang, Xinrun Li, Sizhe Zou, Guoxuan Chi, Siqi Li, Xuchong Qiu, Guoliang Wang, Guantian Zheng, Leichen Wang, Hang Zhao, and Hao Zhao. Chameleon: Fast-slow neuro-symbolic lane topology extraction. In *2025 IEEE International Conference on Robotics and Automation (ICRA)*, pages 3752–3758, 2025. 2
- [46] Yi Zhou, Hui Zhang, Jiaqian Yu, Yifan Yang, Sangil Jung, Seung-In Park, and ByungIn Yoo. Himap: Hybrid representation learning for end-to-end vectorized hd map construction. In *CVPR*, pages 15396–15406, 2024. 3
- [47] Xizhou Zhu, Weijie Su, Lewei Lu, Bin Li, Xiaogang Wang, and Jifeng Dai. Deformable detr: Deformable transformers for end-to-end object detection. In *ICLR*, 2021. 2, 5
- [48] Jannik Zürn, Johan Vertens, and Wolfram Burgard. Lane graph estimation for scene understanding in urban driving. *IEEE Robotics and Automation Letters*, 6(4):8615–8622, 2021. 2

AugMapNet: Improving Spatial Latent Structure via BEV Grid Augmentation for Enhanced Vectorized Online HD Map Construction

Supplementary Material

Overview of Supplementary Material

The supplementary material includes the following parts:

- A. Results on more Perception Ranges
- B. Formulation of Dense Spatial Supervision
- C. Mathematical Definition of Loss Functions
- D. Theoretical Foundation for Gradient Stop
- E. Non-functional Changes with AugMapNet Method
- F. Results on Original nuScenes Split
- G. Results on Argoverse2 for AugMapNet-SQD and Larger Range
- H. Ablation of Kernel Size for Latent BEV Grid Processing CNNs
- I. Additional Qualitative Results
- J. Visualization of Principal Components

A. Results on more Perception Ranges

Tab. 7 shows the results on various perception ranges. Beyond the reported 13.3% improvement on perception range $60\text{ m} \times 30\text{ m}$, we get 19.6% on $80\text{ m} \times 40\text{ m}$, 24.6% on $100\text{ m} \times 50\text{ m}$, 23.4% on $120\text{ m} \times 60\text{ m}$, and 41.4% on $150\text{ m} \times 75\text{ m}$. We find that the relative improvement of AugMapNet increases with larger perception ranges, which suggests a stronger benefit of our augmentation method on wider ranges.

B. Formulation of Dense Spatial Supervision

The loss is calculated over all elements of the output representation $\hat{\mathcal{M}}$. Supervision is done by optimizing a learnable set of weights W based on the gradients of the loss:

$$\frac{\partial L}{\partial W} = \frac{\partial L}{\partial \hat{\mathcal{M}}} \frac{\partial \hat{\mathcal{M}}}{\partial W}. \quad (4)$$

The total amount of spatial supervision therefore is related to the number of elements in $\hat{\mathcal{M}}$.

In the case of a raster map decoder, the predicted output is a rasterized representation: $\hat{\mathcal{M}} = \hat{\mathcal{M}}_{\text{raster}}$. The total gradient signal is calculated from the loss over all pixels. For a raster with spatial resolution $H = 100$ and $W = 50$, this gives a spatial supervision for $|\hat{\mathcal{M}}_{\text{raster}}| = H \times W = 100 \times 50 = 5000$ elements.

In the case of a vector map decoder, the predicted output is a vectorized representation: $\hat{\mathcal{M}} = \hat{\mathcal{M}}_{\text{vector}}$. The total gradient signal is calculated from the loss over all points of all polylines. Our model outputs $N = 100$ polylines, with $N_p = 20$ points each, which gives spatial supervision

Range	Variant	AP _{ped}	AP _{div}	AP _{bound}	mAP	Impr.
$60\text{ m} \times 30\text{ m}^\ddagger$	StreamMapNet [42]	31.2	27.3	42.9	33.8	13.3%
	AugMapNet (ours)	39.4	30.3	45.3	38.3	
$80\text{ m} \times 40\text{ m}^\ddagger$	StreamMapNet [42]	19.4	18.9	24.1	20.8	19.6%
	AugMapNet (ours)	25.9	21.1	27.6	24.9	
$100\text{ m} \times 50\text{ m}^*$	StreamMapNet [42]	25.5	19.3	24.7	23.2	24.6%
	AugMapNet (ours)	35.5	22.8	28.4	28.9	
$120\text{ m} \times 60\text{ m}^*$	StreamMapNet [42]	19.29	10.95	12.79	14.34	23.4%
	AugMapNet (ours)	24.13	12.72	16.26	17.70	
$150\text{ m} \times 75\text{ m}^*$	StreamMapNet [42]	10.5	6.4	3.9	6.9	41.4%
	AugMapNet (ours)	15.2	7.5	6.7	9.8	

Table 7. Results on nuScenes dataset [1] on more perception ranges. AP thresholds ‡ : {0.5, 1.0, 1.5}, * : {1.0, 1.5, 2.0}.

for at most $|\hat{\mathcal{M}}_{\text{vector}}| = N \times N_p = 100 \times 20 = 2000$ elements. Note that, in DETR-style decoders, elements that are correctly predicted as empty class do not induce spatial supervision. Hence, this number is the upper bound and the actual supervision is typically even sparser.

We believe that this difference in the number of elements is why integrating dense spatial supervision into vectorized map decoding is so effective.

C. Mathematical Definition of Loss Functions

The formulation of the vector map decoder loss, $\mathcal{L}_{\text{vector}}$, is taken from StreamMapNet [42] and consists of multiple components. As the first step of the polyline matching loss, $\mathcal{L}_{\text{line}}$, bipartite matching is performed between predicted and GT polylines. After matching, the smooth L1 loss is calculated for each of the N_p points P_j of the matched polyline P . The best one in the permutation group, Γ , as introduced in MapTR [19], is used:

$$\mathcal{L}_{\text{line}}(\hat{P}, P) = \min_{\gamma \in \Gamma} \frac{1}{N_p} \sum_{j=1}^{N_p} \mathcal{L}_{\text{SmoothL1}}(\hat{P}_j, P_{\gamma(j)}). \quad (5)$$

The classification loss, $\mathcal{L}_{\text{class}}$, calculates the loss between the ground truth class vector, c , and predicted class vector, \hat{c} , for each polyline. The loss function is the Focal loss:

$$\mathcal{L}_{\text{class}}(\hat{c}, c) = \mathcal{L}_{\text{Focal}}(\hat{c}, c). \quad (6)$$

An auxiliary transformation loss, $\mathcal{L}_{\text{trans}}$, is used to match the ego-motion transformation in latent space. Given a standard 4×4 transformation matrix, T , between the coordinate frames of $t - 1$ and t , the polyline of the vector map at time t is expressed as $P = T \cdot \text{homogeneous}(P')_{:,0:2}$, where P' is the polyline of the vector map at time $t - 1$. For a

query in the vector map decoder at time t , Q , an auxiliary prediction is made with $\hat{P}^{\text{aux}} = \text{Reg}(Q)$. The auxiliary transformation loss is then defined as:

$$\mathcal{L}_{\text{trans}}(\hat{P}^{\text{aux}}, P) = \sum_{j=1}^{N_p} \mathcal{L}_{\text{SmoothL1}}(\hat{P}_j^{\text{aux}}, P_j). \quad (7)$$

The final loss is a weighted sum of the above loss terms with the factors $\lambda_1 = 50.0$, $\lambda_2 = 5.0$, and $\lambda_3 = 0.1$ over all predicted polylines in $\hat{\mathcal{M}}_{\text{vector}}$:

$$\mathcal{L}_{\text{vector}} = \sum_{P \in \hat{\mathcal{M}}_{\text{vector}}} (\lambda_1 \mathcal{L}_{\text{line}} + \lambda_2 \mathcal{L}_{\text{class}} + \lambda_3 \mathcal{L}_{\text{trans}}). \quad (8)$$

The raster map decoder loss $\mathcal{L}_{\text{raster}}$ is the Dice loss [25]:

$$\mathcal{L}_{\text{raster}}(\hat{\mathcal{M}}_{\text{seg}}, \mathcal{M}_{\text{seg}}) = \mathcal{L}_{\text{Dice}}(\hat{\mathcal{M}}_{\text{seg}}, \mathcal{M}_{\text{seg}}). \quad (9)$$

D. Theoretical Foundation for Gradient Stop

We provide more analysis on gradient stopping to provide a theoretical foundation for the benefits that we observed empirically. We start our reasoning from the results of the ‘‘Oracle’’ experiment (see details of experiment in Sec. 4.7).

The result of 91.4% mAP shows that given a perfect raster map, the injection of dense spatial features in our AugMapNet method can yield a close-to-perfect result on the vectorized map construction. We denote using this perfect raster map, that reaches the *empirical upper bound* in the ‘‘Oracle’’ experiment, as $\hat{\mathcal{M}}_{\text{raster}} = \mathcal{M}_{\text{raster}}^*$. In practice, the predicted raster map includes residual error η , such that $\hat{\mathcal{M}}_{\text{raster}} = \mathcal{M}_{\text{raster}}^* + \eta$. Without gradient stopping ∇e_{raster} is active, backpropagating gradients from the vector loss $\mathcal{L}_{\text{vector}}$ to d_{raster} . Therefore, instead of purely optimizing for a perfect raster map, $\frac{\partial \mathcal{L}_{\text{vector}}}{\partial W_{d_{\text{raster}}}}$ biases d_{raster} toward vector-specific features, increasing $\|\eta\|$.

E. Non-functional Changes with AugMapNet Method

This section provides more details on the non-functional changes when applying our AugMapNet method to StreamMapNet. Our AugMapNet method has only a small effect on the model size in VRAM. We observe ≈ 1.8 GB for either of them. During training on batch size 1, we see a VRAM usage of ≈ 7.7 GB, a slight increase of 1.6%. Train time also increases slightly from 14.5 h to 15.4 h (6%). Inference takes 78 ms vs. 70 ms, an 11% increase. AugMapNet still meets real-time requirements with 11.9 FPS.

F. Results on Original nuScenes Split

The original nuScenes Split is still commonly used to train and evaluate approaches for online map construction. For completeness, the results on the original split are shown

Method	AP _{ped}	AP _{div}	AP _{bound}	mAP	Impr.
VectorMapNet [21]	36.1	47.3	39.3	40.9	
MapTR [18]	46.3	51.5	53.1	50.3	
MapTRv2 [19]	59.8	62.4	62.4	61.5	
MapVR [43]	47.7	54.5	51.4	51.2	
MGMap [20]	57.4	63.5	63.3	61.4	
StreamMapNet [42]	60.2	65.1	61.1	62.1	
AugMapNet (ours, ∇e_{raster} off)	60.8	65.7	61.7	62.7	1.0%
AugMapNet (ours, ∇e_{raster} on)	61.9	65.4	63.6	63.6	2.4%
StreamMapNet 100x50 [42]	63.5	64.9	57.1	61.8	
AugMapNet 100x50 (ours)	66.1	64.1	60.0	63.4	2.5%
SQD-MapNet [39]	62.2	67.0	65.4	64.9	
AugMapNet-SQD (ours)	64.1	65.0	67.8	65.6	1.1%
SQD-MapNet 100x50 [39]	62.9	65.8	61.4	63.3	
AugMapNet-SQD 100x50 (ours)	67.3	68.6	63.7	66.5	3.5%

Table 8. Results on original nuScenes [1] split with geospatial overlap. Results from baselines are taken from the respective papers. Values are much higher compared to geospatially disjoint split due to overfitting.

in Tab. 8. Comparing the absolute values to the results on the geospatially disjoint split (*cf.* Tab. 1) reveals severe overfitting due to geospatial overlap: StreamMapNet result increases from 33.8% mAP to 62.1% mAP, an 84% jump due to overfitting. AugMapNet overfits less with only 64% higher mAP (62.7% mAP on old vs. 38.3% mAP on geospatially disjoint splits). Thanks to less overfitting, AugMapNet improvements are smaller on the old split, though still substantial. A primary reason is gradient stopping: turning off ∇e_{raster} improves performance on the geospatially disjoint split (*cf.* Sec. 4.7) but not on the old split (62.7% mAP without ∇e_{raster} vs. 63.6% mAP without ∇e_{raster}). Consistent with the results on the geospatially disjoint split, AugMapNet shows an even stronger improvement on larger perception ranges with 2.5% when evaluated on 100 m \times 50 m range on the original split (*cf.* Tab. 3 and Tab. 8).

We follow best practices in ML to only perform comparisons on truly unseen evaluation data (*i.e.*, the geospatially disjoint split). For completeness, other baselines are added to Tab. 8. We note that comparison of absolute values mainly depends on the choice of baseline. Once code for the latest state-of-the-art models is available, AugMapNet can easily be integrated to further advance them.

G. Results on Argoverse2 for AugMapNet-SQD and Larger Range

This section extends upon the results of AugMapNet on Argoverse2 (see Tab. 2). To assess how well our method generalizes across datasets and sensor configurations on different ranges, we extend Tab. 2 by adding 100 m \times 50 m range. Beyond the 3.0% improvement on 60 m \times 30 m range, we observe 3.4% improvement on 100 m \times 50 m range.

To assess how well our method generalizes not only across datasets and sensor configurations, but also across

Range	Method	AP _{ped}	AP _{div}	AP _{bound}	mAP	Impr.
60 m × 30 m [‡]	StreamMapNet [42]	56.0	54.4	61.0	57.1	3.0 %
	AugMapNet (ours)	57.4	57.4	61.6	58.8	
100 m × 50 m*	StreamMapNet [42]	57.9	44.4	47.5	49.9	3.4 %
	AugMapNet (ours)	60.6	44.8	49.4	51.6	
60 m × 30 m [‡]	SQD-MapNet [39]	58.3	54.7	62.2	58.4	4.3 %
	AugSQD (ours)	60.0	58.0	64.6	60.9	
100 m × 50 m*	SQD-MapNet [39]	59.2	45.9	49.7	51.6	6.2 %
	AugSQD (ours)	63.3	49.7	51.4	54.8	

Table 9. Results on different perception ranges for AugMapNet and application of our method to SQD-MapNet [39] denoted as AugSQD. Results are on Argoverse2 split without geospatial overlap [1]. AP thresholds [‡]: {0.5, 1.0, 1.5}, *: {1.0, 1.5, 2.0}.

Index	Kernel	# Layers	AP _{ped}	AP _{div}	AP _{bound}	mAP
a)	-	0	31.2	27.3	42.9	33.8
b)	1	1	36.6	30.3	41.4	36.1
c)	3	1	36.4	30.0	43.7	36.7
d)	5	1	33.9	30.3	43.8	36.0

Table 10. Ablation of kernel size of BEV processing CNNs. a) is StreamMapNet [42].

models without any changes, we train AugMapNet-SQD (“AugSQD”) on the Argoverse2 dataset [40] and show the results in Tab. 9. AugMapNet-SQD reaches 60.9 % mAP on 60 m × 30 m range, a 4.3 % improvement over SQD-MapNet. On 100 m × 50 m range, AugMapNet-SQD reaches 54.8 % mAP, an even higher improvement of 6.2 % The improvements are substantial and even higher than the 3.0 % improvement of AugMapNet over StreamMapNet on Argoverse2 (*cf.* Tab. 2), confirming the broader applicability of our method. Furthermore, the values show an increase in relative improvement at larger perception ranges a fifth time (*cf.* Tab. 3 and Tab. 8).

H. Ablation of Kernel Size for Latent BEV Grid Processing CNNs

In this study, shown in Tab. 10, we investigate the effect of kernel size by comparing sizes of 1, 3, and 5 (*b*, *c*, *d*, resp.) on nuScenes. Similar to Sec. 4.8, here we do not use our BEV augmentation. Size 3 is used for further experiments since it gives the best result with 36.7 % mAP.

I. Additional Qualitative Results

We provide further qualitative results to highlight the benefits of AugMapNet.

A separate video file is included with this submission to show the performance of AugMapNet on a full scene. It overlays the predicted vector map polylines in each camera view to visualize the spatial accuracy.

Fig. 6 shows a scene where StreamMapNet misses the road divider on the left side of the ego vehicle. AugMapNet predicts the road divider to include a roadway turnout,

which is reasonable given the large driveway that is occupied by a truck. Fig. 7 shows a scene where a traffic island and a crosswalk to the front-left of the ego vehicle are missed by StreamMapNet, but correctly predicted by AugMapNet. Fig. 8 visualizes a rainy scene to show model performance under challenging weather conditions, including a rain droplet on the front-facing camera lens that limits visibility. StreamMapNet misses a crosswalk in the area that AugMapNet predicts correctly. Fig. 9 shows a scene at night with limited illumination. AugMapNet predicts the left road boundary fairly accurately given the visibility, whereas StreamMapNet misses it completely.

J. Visualization of Principal Components

As an extension to the top 3 Principal Components (PCs) visualized in Fig. 4, we visualize the top 16 PCs for example scene 1 in Fig. 10 and for example scene 2 in Fig. 11. A general observation is that the PCs tend to have more radial artifacts in StreamMapNet. The PCs of AugMapNet have better spatial structure and correspondence with the GT map due to dense spatial supervision.

Finally, Fig. 12 gives more details on example scene 1, where StreamMapNet misses a pedestrian crossing that is correctly predicted by AugMapNet. Specifically, we highlight the PC that has the highest visual correspondence to the pedestrian crossing GT out of the top 16 PCs visualized in Fig. 10 for each StreamMapNet and AugMapNet. It is PC 14 for StreamMapNet and PC 8 for AugMapNet. The smaller number for AugMapNet indicates that AugMapNet has stronger latent features for pedestrian crossings, which likely helped with its correct prediction. This also matches the better visual correspondence between the AugMapNet PC and the pedestrian crossing GT compared to StreamMapNet.

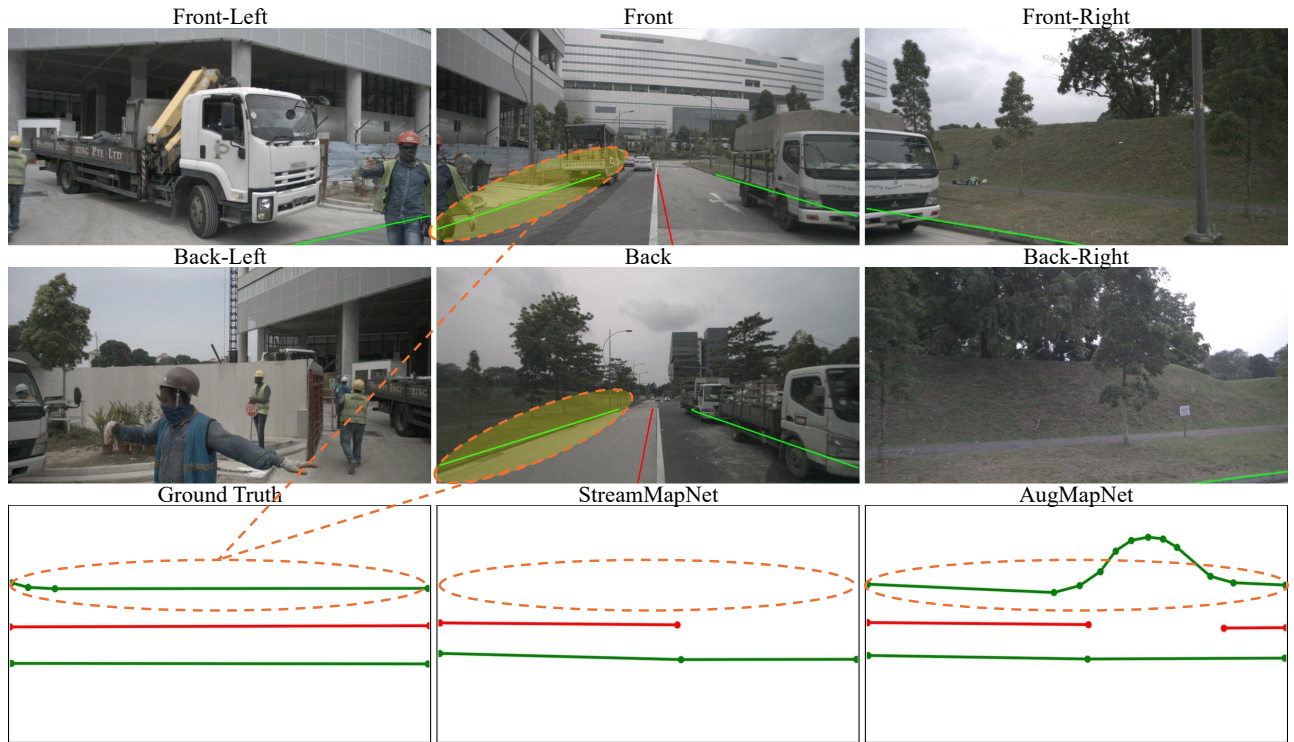


Figure 6. Qualitative results for example scene 3 with an extensive driveway on the left side. Lane dividers are red, road boundaries are green, and pedestrian crossings are blue.

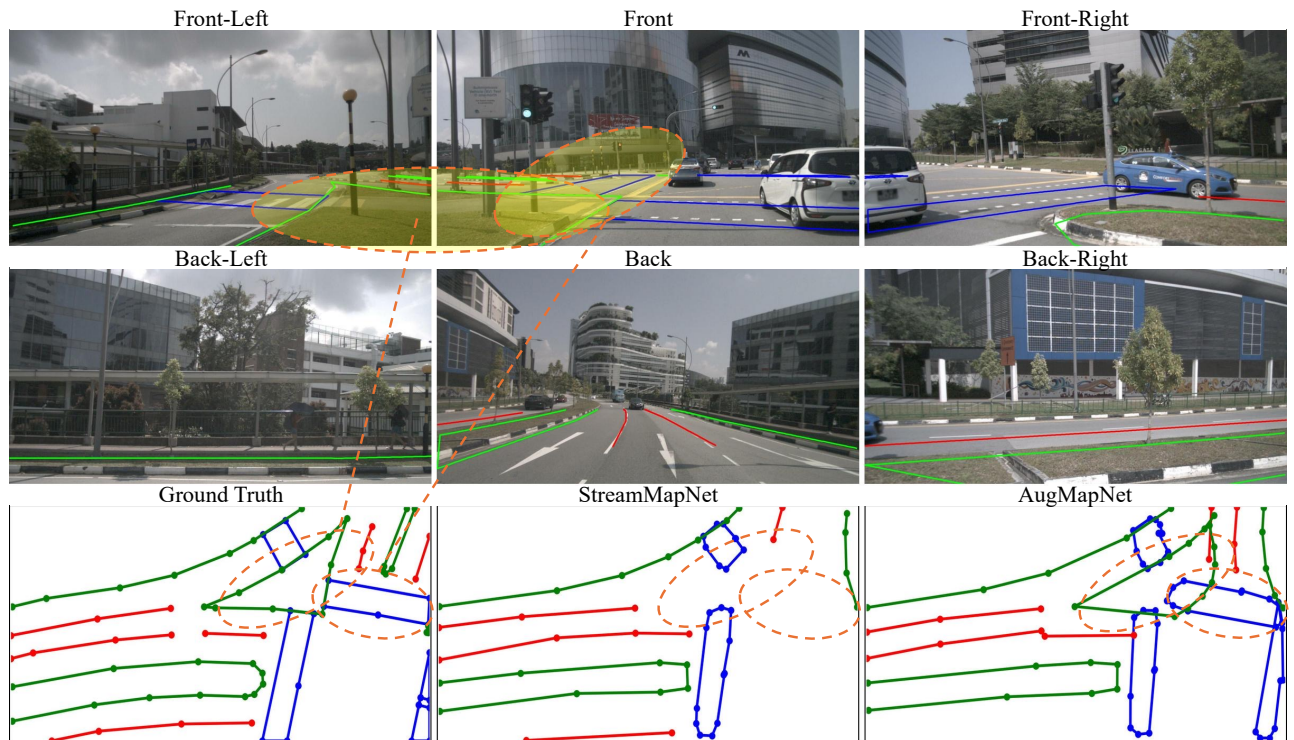


Figure 7. Qualitative results for example scene 4 with traffic island and pedestrian crossing on the left. Lane dividers are red, road boundaries are green, and pedestrian crossings are blue.

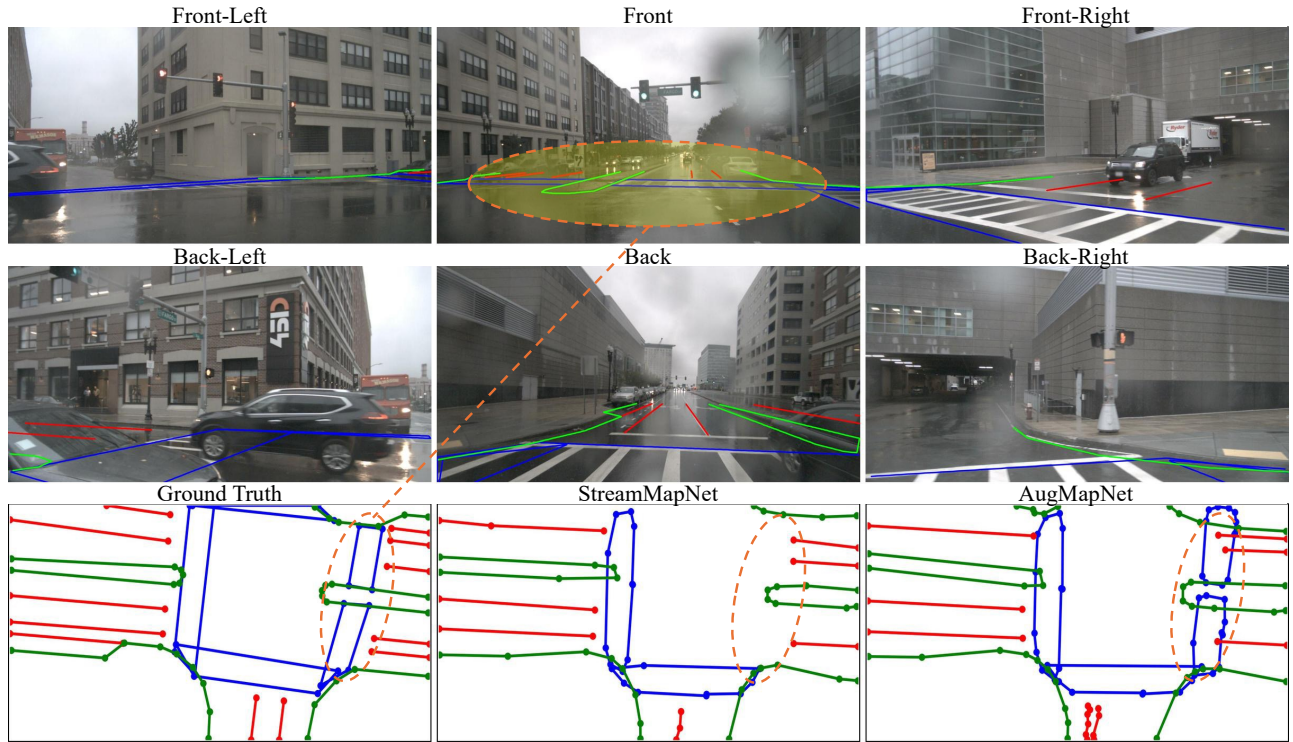


Figure 8. Qualitative results for example scene 5 under rainy conditions. Lane dividers are red, road boundaries are green, and pedestrian crossings are blue.

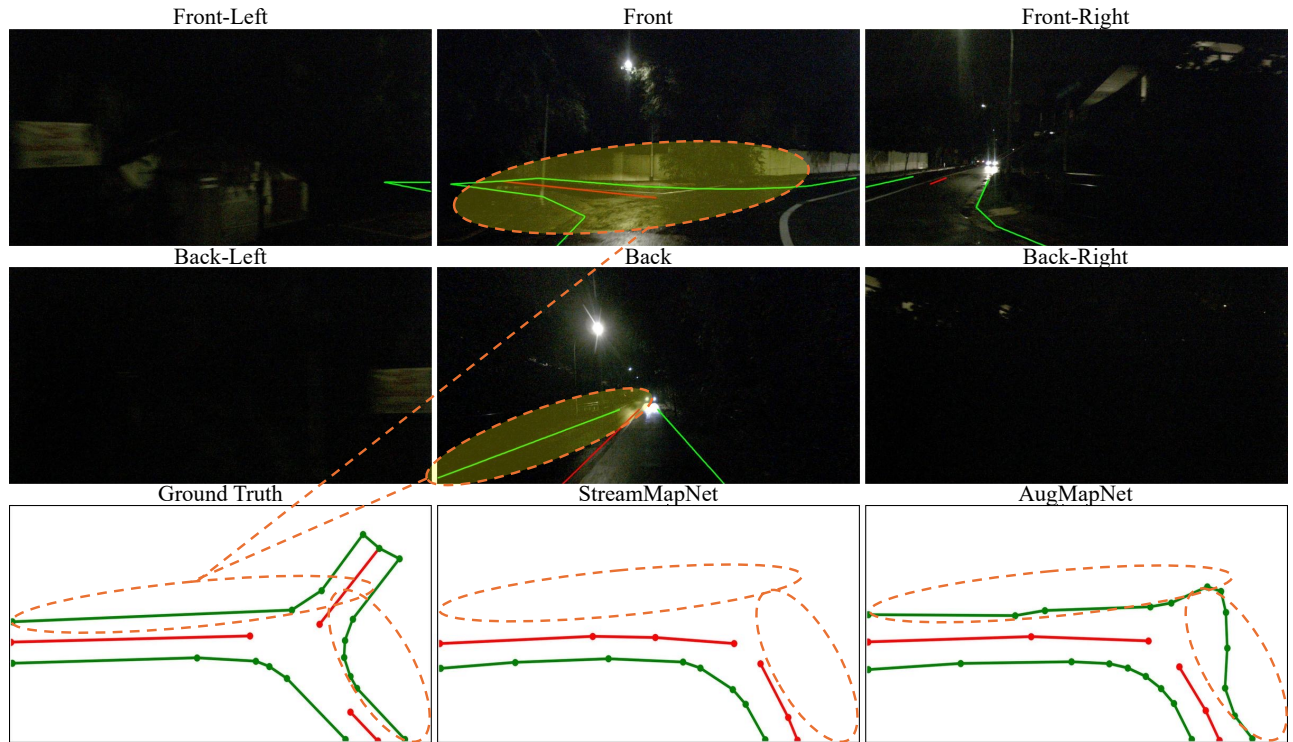
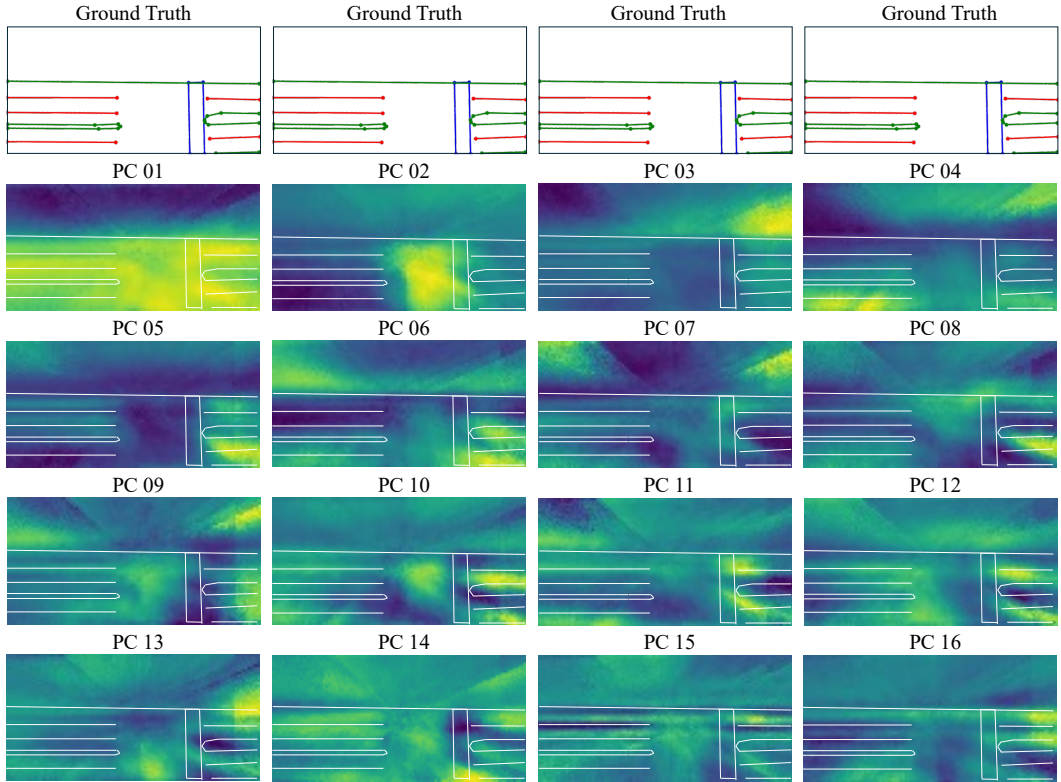
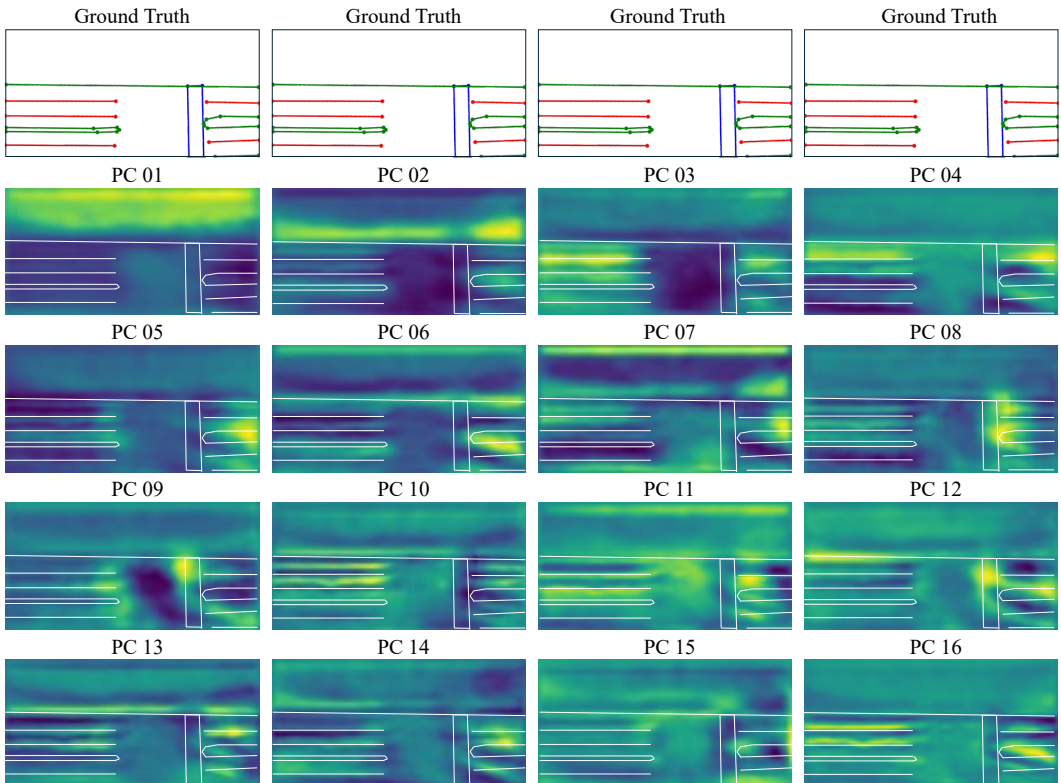


Figure 9. Qualitative results for example scene 6 with limited illumination. Lane dividers are red, road boundaries are green, and pedestrian crossings are blue.

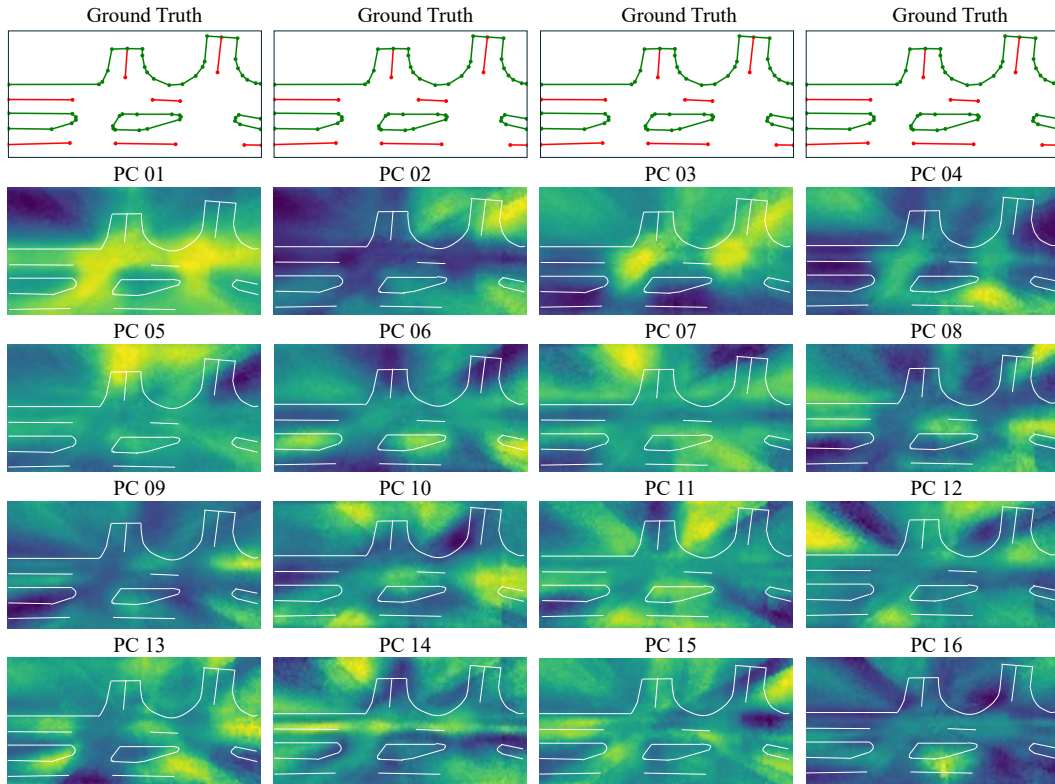


(a) StreamMapNet

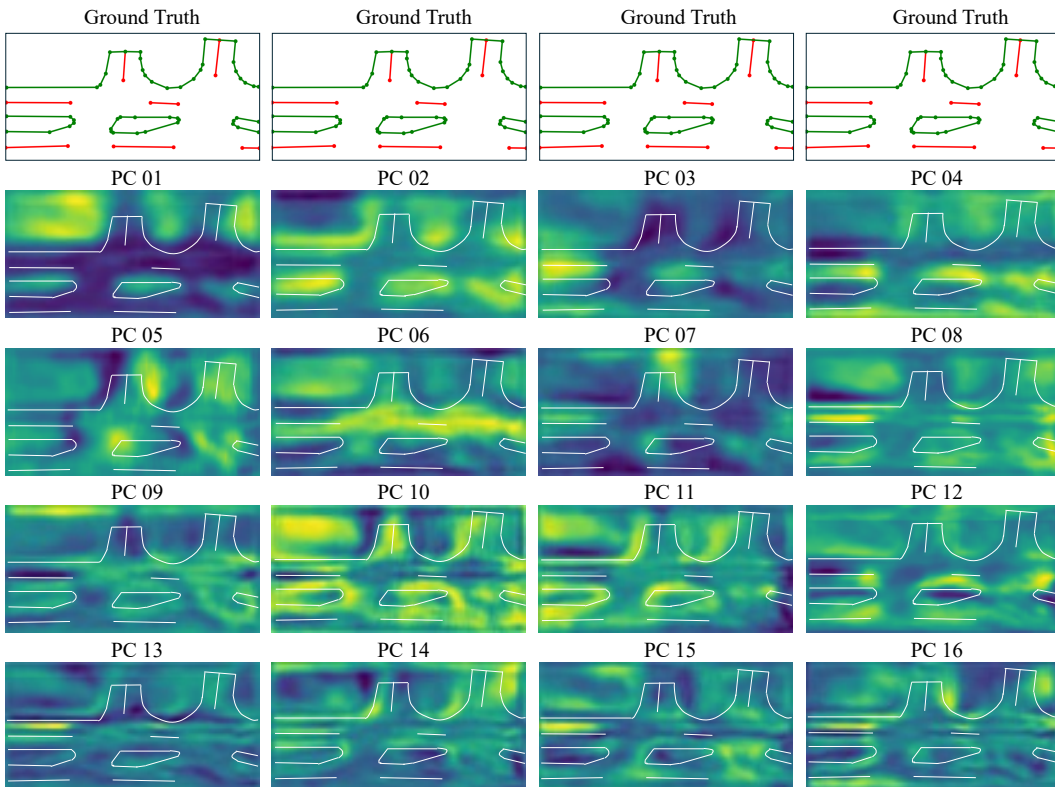


(b) AugMapNet

Figure 10. Example scene 1: Top 16 Principal Components of latent BEV grid of (a) StreamMapNet and (b) AugMapNet. Vector map ground truth is visualized at the top of each column as well as overlaid as white lines to ease the assessment of spatial accuracy. Notice that StreamMapNet tends to have radial artifacts.



(a) StreamMapNet



(b) AugMapNet

Figure 11. Example scene 2: Top 16 Principal Components of latent BEV grid of (a) StreamMapNet and (b) AugMapNet. Vector map ground truth is visualized at the top of each column as well as overlaid as white lines to ease the assessment of spatial accuracy. Notice that StreamMapNet tends to have radial artifacts.

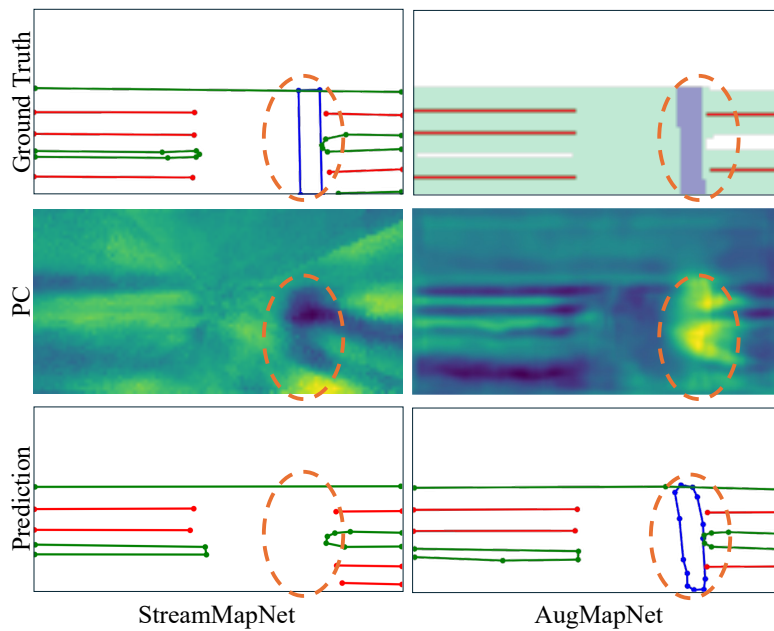


Figure 12. Extension of Fig. 4, visualizing example scene 1 where pedestrian crossing is missed by StreamMapNet but predicted by AugMapNet. PC is the Principal Component of the BEV latent grid that has the highest visual correspondence to the pedestrian crossing out of the top 16 Principal Components visualized in Fig. 10. It is PC 14 for StreamMapNet and PC 8 for AugMapNet, suggesting that this “crossing” PC is stronger in AugMapNet than StreamMapNet.